Journal of Materials Chemistry A

Accepted Manuscript

ROYAL SOCIETY OF CHEMISTRY

www.rsc.org/materialsA

Table of Contents

Ordered mesoporous Ag-doped TiO_2/SnO_2 nanocomposite based highly sensitive and selective VOCs sensor

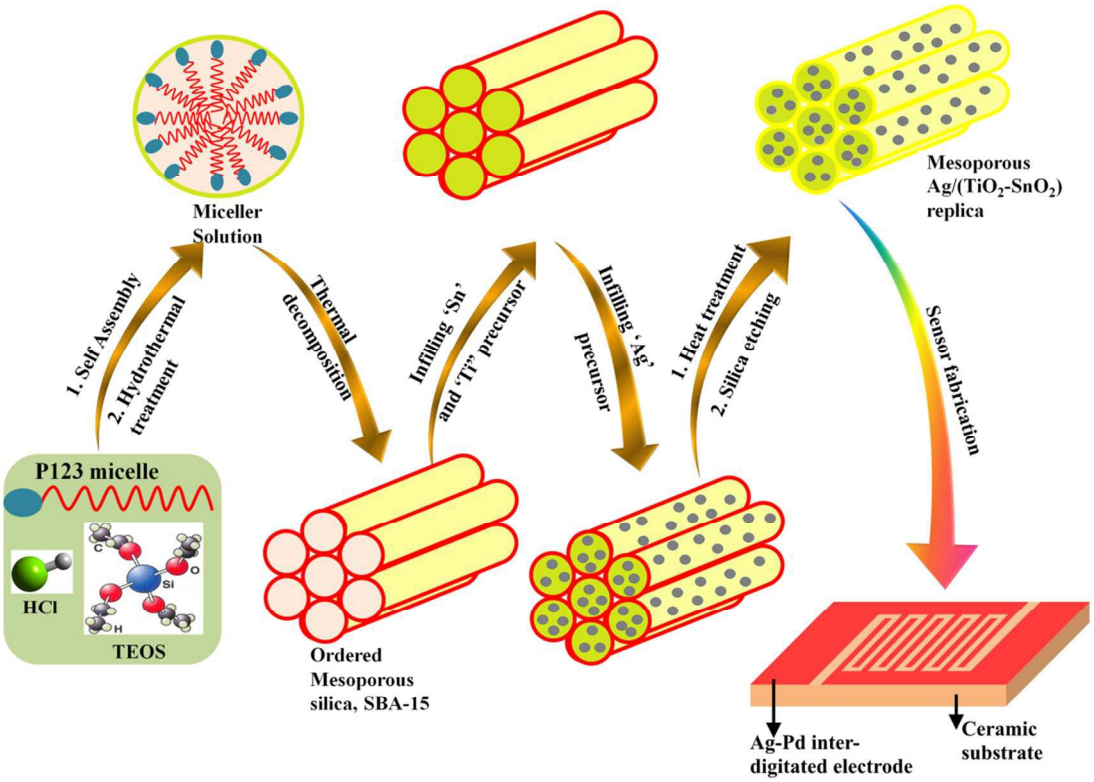

Highly ordered Ag-(TiO_2/SnO_2) nanocomposite synthesized as a result of negative replica of mesoporous SBA-15 framework shows excellent ethanol sensing property

Ordered mesoporous Ag-doped TiO_2/SnO_2 nanocomposite based highly sensitive and selective VOCs sensor

Vijay K. Tomer and Surender Duhan*

Nanomaterials Research Laboratory

Department of Materials Science & Nanotechnology

D.C.R. University of Science & Technology, Murthal (Sonepat) Haryana, 131039 (INDIA)

Abstract

Hybrid mesoporous metal oxides shows promising attributes in the field of relative gas sensors due to the combined opportunities provided by high specific surface area and framework components. In this study, we present the synthesis of ordered mesoporous tin (IV) oxide–titanium (IV) oxide nanohybrid using a sequential combination of two-step wet impregnation and nanocasting process and demonstrate response by exposing the mesoporous nanohybrids to ethanol at room temperature. HRTEM and N_2 adsorption–desorption results indicates that the nanohybrid prepared using nanocasting of SBA-15 as hard template possess ordered mesoporous structure and high surface area. It was also observed that the mesoporous Ag-(TiO_2/SnO_2) shows good response towards ethanol with the concentrations ranging from 1 ppm to 500 ppm. Besides, the nanohybrid mesoporous sensor shows high selectivity towards other volatile organic compounds (VOCs) including acetone, methanol, isopropanol and benzyl alcohol. All the results indicated that the nanocasted mesoporous Ag-(TiO_2/SnO_2) nanohybrids have a great potential for application in designing high performance practical ethanol sensors.

Keywords: Nanocasting, hard template, ethanol, mesoporous, TiO_2/SnO_2

* **Corresponding author**

E-mail: surender6561@yahoo.co.in

Tel.: +91- 9813170944.

Introduction

Volatile organic compounds (VOCs) are known to possess high vapor pressure at ordinary room temperature. They are the antecedents of photochemical smog, ozone, and auxiliary aerosol, and are unsafe to human being due to their poisonous, mutagenic, teratogenic, cancer-causing and rotten nature.[1,2] VOCs are considered as significant contributors to indoor air pollution; and bring about both short-and long haul on human health as well as on the natural ecosystem. Unconstrained breathing of VOCs prompts various ailments in kids and elderly people particularly those having asthma, allergies, or other respiratory illness and causes uncommon dangers.[3,4] Therefore, the development of efficient, low-cost, ultrasensitive, highly selective and convenient chemical sensors which can precisely recognize and measure the presence of VOCs and human exposure levels have become a significant endeavor for the wellbeing and welfare of people and safety and process control in industrial applications.[5,6]

In the last decade, hybrid metal oxides with mesoporous structures have attracted much attention due to their attractive properties and potential in detecting indoor air pollution caused by VOCs.[7,8] Mesoporous materials with large intrinsic surface area and wide pore diameters are able to facilitate physical/chemical adsorption and immobilization of gas molecule in the pore channels.[9,10] Hybrid metal oxides, wherein, constitutive components are responsible for high sensitivity and response, the additional provision of mesoporosity can provide desirable high accessible surface area and adequate diffusion of gas molecules/charge carriers to the active sites.[11,12] Recently, the templated synthesis by means of nanocasting procedure has made a vogue progress in synthesizing ordered mesoporous materials with controlled composition and physico-chemical properties. These hard templated (or 'nanocasted') materials are different from those prepared using conventional co-precipitation, sol-gel or hydrothermal routes in terms of their internal surface area, mesoporosity and crystalline pore walls.[13,14] A diverse range of metal

oxides such as NiO, CO_3O_4, V_2O_5, WO_3, $LaFeO_3$, and SnO_2 with ordered 2D mesoporous structures, high crystallinity and large surface area have been successfully prepared by using nanocasting method for detecting a variety of gases.[15-19] Among these metal oxides, Tin oxide (SnO_2), a wide bandgap (~3.7 eV) n-type semiconductor with excellent electrical and optical properties has gained particular attention as promising sensor material for detecting a variety of gases.[20-23] It is well known that the internal surface area of the material have a significant impact on their sensing properties. Therefore, extensive research has been implied for preparing diverse morphologies of SnO_2 with increased surface area, such as core shell nanostructures, nanorod, nanoflowers, hollow spheres, nanosheets, nanofibers, nanospheres, microcubes and hierarchical nanostructures, for utilization in sensing and photocatalytic applications.[24-27] Ordered mesoporous SnO_2 with regular porosity and large specific surface area have a lot of advantages as compared to their bulk counterparts in the field of gas sensors due to the provision of high accessibility for the gas analytes across the sensor surface alongside the presence of enormous amount of surface active sites for the surface-chemical interaction between the gas molecules and SnO_2 materials.[13,19]

One effective approach for the development of efficient sensors lies in the modulation of properties of SnO_2 by coupling with other semiconducting materials to form heterostructures.[1,7,8,12,23,24] In particular, Sun et al. have synthesized α-Fe_2O_3 nanosheets hierarchically assembled on SnO_2 hollow nanospheres for detecting a variety of VOCs.[24] The nanostructures possess high surface area and pore volume and are particularly found responsive towards detection of ethanol gas. Weng et al. have synthesized coral like Zn-doped SnO_2 nanostructures with high surface area and determine the high selectivity of the synthesized material towards detection of butanone among a variety of different VOCs.[12] Rakshit et al. have reported the synthesis of ZnO-SnO_2 heterostructures for detecting acetone among several VOCs.[23] Similarly, Nayak et al. have used a

simple hydrothermal method to prepare porous WO_3-SnO_2 nanohybrid.[1] They have observed temperature dependent response of sensor towards various VOCs. A few studies have reported that the addition of TiO_2 into SnO_2 could improve the heterojunction based properties of the composite for utilization in gas sensing applications. This could be attributed to the easier substitution of Sn ions by Ti ions due to the similar ion radius of Ti^{4+} and Sn^{4+} (Ti^{4+} 0.61Å, Sn^{4+} 0.69 Å), which may produce more oxygen vacancies for charge compensation thereby increasing the sensing performance of SnO_2.[28,29]

Considering the effectiveness of TiO_2 and SnO_2 nanostructures for sensing different gases, we report here the nanocasting synthesis of highly ordered mesoporous Ag doped TiO_2/SnO_2 nanocomposite by using SBA-15 hard template for selective detection of VOCs. Ag nanoparticles, because of their excellent chemical/ biological sensing properties, high stability, conductivity and ability to accelerate chemical reaction process,[30,31] were used to enhance the sensing response of TiO_2/SnO_2 nanocomposite. The gas sensing properties of the mesoporous Ag-(TiO_2/SnO_2) nanostructures were investigated by measuring the response of sensor in detecting important representative VOCs such as ethanol, methanol, acetone, isopropanol, benzyl alcohol and ethyl acetate. The mesoporous nanocomposite based sensor exhibited a high response, excellent reproducibility, quick response/recovery characteristics and good selectivity to ppm-level ethanol which provide a promising opportunity to exploit the use of mesoporous materials in designing futuristic commercial sensors.

Experimental

Materials

Tetraethoxy orthosilicate ($(C_2H_5O)_4Si$, TEOS, Sigma Aldrich), Pluronic P123 (Ethylene Oxide-Propylene Oxide-Ethylene Oxide, ($EO_{20}PO_{70}EO_{20}$), M_w = 5800 g/mol, Sigma Aldrich), Tin (II) chloride ($SnCl_2$•$2H_2O$, Merck), Titanium tetrachloride ($TiCl_4$, Merck), Silver Nitrate ($AgNO_3$, Fisher Scientific), Polyethylene glycol (PEG-200, Merck), Sodium Hydroxide (NaOH, Fisher

Scientific), Ethanol (Fisher Scientific) and HCl (35%, Fisher Scientific) were used as received. Double distilled water was used throughout the experiments.

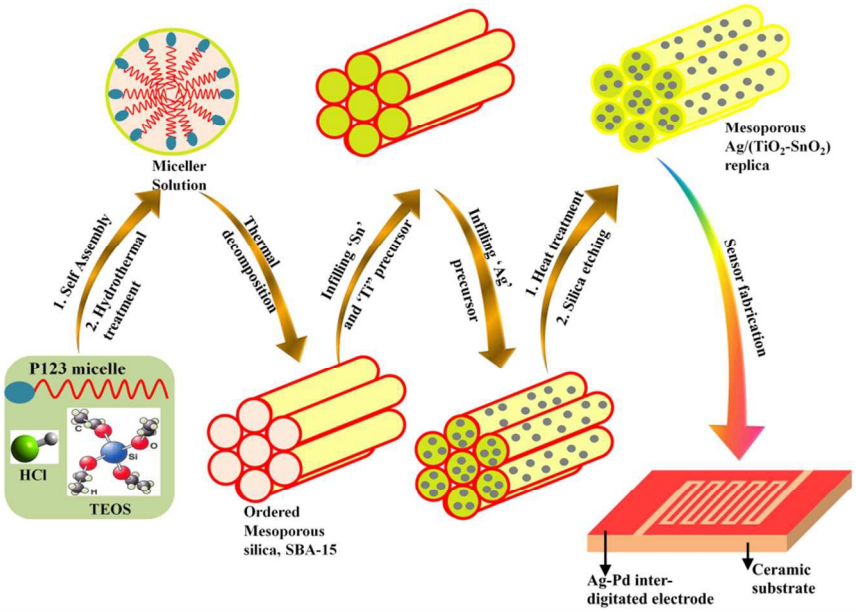

Fig 1: Schematic representation for nanocasting synthesis of ordered mesoporous Ag-(TiO_2/SnO_2) by hard templating of SBA-15.

Material Preparation

SBA-15 was synthesized using a method described elsewhere.[31] For the nanocasting synthesis of ordered mesoporous TiO_2/SnO_2 using SBA-15 as hard template (Fig 1), 1g of SBA-15 was dispersed in 20 ml of ethanol. After stirring at 40 °C for 1 h, 0.8g $SnCl_2$•$2H_2O$ were added to the solution followed by the addition of 0.2 ml $TiCl_4$ and the stirring continues till all the ethanol was evaporated. Afterwards, the resulting powder was heated at 600 °C (heating rate 2 °C/min) for 6 h to convert tin chloride and titanium chloride to tin dioxide and titanium oxide within the pores of SBA-15 template. The process of pore filling and heating were repeated twice following the same conditions in order to achieve higher loadings of dopants. Finally, the silica template was removed at room temperature using 2M of 50 ml NaOH solution. The white TiO_2/SnO_2 material was recovered, washed with distilled water and dried at 70 °C overnight to obtain pure ordered mesoporous TiO_2/SnO_2 nanostructures.

Ordered mesoporous Ag-(TiO_2/SnO_2) nanostructures (2wt% Ag to SnO_2) were obtained by following similar procedure as described for TiO_2/SnO_2 composite along with the addition of 0.17 g $AgNO_3$ in the solution of SBA-15 (1g), ethanol (20 ml), $SnCl_2$•$2H_2O$ (0.8g) and $TiCl_4$ (0.2 ml). Afterwards, the final Ag-(TiO_2/SnO_2) nanocomposites were obtained by following the same procedure as described above for the synthesis of TiO_2/SnO_2 nanostructures.

For comparison, TiO_2/SnO_2 nanocomposite (soft template) was also synthesized by the hydrothermal method using conventional surfactants. In a typical procedure, 1 ml $TiCl_4$ was mixed into 20 ml (1M) solution $SnCl_2$•$2H_2O$ under stirring. Then, 30 ml (1M) NaOH was added dropwise to obtain a clear solution. After 2 h, 10 ml PEG was added to the above solution followed by the addition of 20 ml ethanol. Then resultant solution was transferred to a Teflon lined stainless steel autoclave and maintained at 170 °C for 24h, which was later allowed to cool down naturally at room temperature. The white powder precipitates were recovered, filtered off, washed four times with distilled water and dried overnight at 80°C to obtain TiO_2/SnO_2 composites. For the ease of analysis, samples SBA-15, TiO_2/SnO_2 (soft template), TiO_2/SnO_2 (hard template) and Ag-(TiO_2/SnO_2) were denoted as S-15, TS-s, TS-h, ATS-h respectively. The suffixes '-s' and '-h' stands for nanocomposite sample synthesized using soft template and hard template respectively.

Fabrication and performance test of gas sensors

The ceramic substrates having 5 tracks of Ag-Pd electrodes (13.4mm x 7mm x 0.5mm) and electrode width and separation distance of 0.2 mm was used to study sensing response in this work (Fig 1). A grounded and diluted paste of sample/distilled water in 1:20 weight ratio was dropped on the substrate using a 10 µL pipette. The substrate was then heated in oven for 10 h at 60 °C to form a sensing film of thickness ~5 µm. The measurements were carried out in a custom made gas sensing set-up. The set-up contains air sealed stainless steel chamber equipped with a

heater, thermocouple, and probes. The gas sensing proceeds by following a static process wherein a definite amount of the target gas was injected into a closed glass chamber, where sensor was placed to evaluate its sensing performance. The desired concentration of the targeted gas was obtained by the static liquid gas distribution method, which was calculated by the following formula,[32]

$$C = \frac{22.4 \times \phi \times \rho \times V_1}{M \times V_2} \times 1000$$

where C (ppm) is the target gas concentration, ϕ the required gas volume fraction, ρ (g/mL) the density of the liquid, V_1 (μL) the volume of liquid, V_2 (L) the volume of the chamber, and M (g/mol) the molecular weight of the liquid. The gas response (R) was defined as the ratio R_a/R_g, where R_a and R_g were the resistances measured in air and the tested gas atmosphere. The response and recovery time were defined as the time taken by the sensor to achieve 90% of the total resistance change in the case of adsorption and desorption, respectively.

Characterization of materials

X-ray diffraction (XRD) data were recorded on a Bruker D8 Advance X-ray diffraction instrument with Cu-K_α monochromatic radiation (λ = 0.154 nm) with 40 kV voltage and 40 mA. The diffraction patterns were collected over 2θ range, between 0.5–3.0° and 15–70° for small angle and wide-angle measurements respectively. N_2 adsorption-desorption isotherms were measured on Micromeritics (Tristar 3000) at 77 K. Before measurements, a known mass of sample (~ 150 mg) was degassed overnight under vacuum at 300 °C. The specific surface area was calculated by the five point Brunauer-Emmett-Teller (BET) method,[33] in the range 0.05 to 0.2 of relative pressure and the pore size distribution was derived from the desorption branch of the isotherms by using the Barrett-Joyner-Halenda (BJH) analysis.[34] The information regarding the mesoporosity and order channels along with its elemental composition were characterized by

a High resolution transmission electron microscope (HRTEM) instrument (TECNAI G20) at an acceleration voltage of 200 kV which is equipped with an Energy-dispersive X-ray (EDX) spectroscope. X-Ray photoelectron spectra (XPS) of the sensor was recorded in PHI 5000 Versa Prob system using Al Kα (1486.6 eV) radiation operating at an accelerating power of 15 kW. Before performing the scan, the sample was outgassed in a UHV chamber (< 5×10^{-7} Pa) at room temperature. The spectra were referenced to the binding energy of C (1s) (285 eV).

Results and Discussion

Characterization

The order mesoporous TiO_2/SnO_2 and Ag-(TiO_2/SnO_2) were synthesized using SBA-15 as hard template according to the nanocasting concept in which the pore channels of SBA-15 were filled with precursor salt and the mesoporous negative replica of respective metal oxide(s) was recovered later on by using NaOH as etchant for removal of SBA-15. The sequential loading of guest species in SBA-15 facilitates the entrance of initial species inside the pore channels of SBA-15 while this tendency decreases with loading of the subsequent species due to the hindrance caused by already filled pore channels. In the present work, the pore channels of SBA-15 were filled easily with $SnCl_2{\bullet}2H_2O$ species. The already filled pore channels of SBA-15 offers hindrance to the impregnation of $TiCl_4$ and hence $TiCl_4$ species partially resides in and surface of SBA-15 pore channels. Also, the possibility of $AgNO_3$ species to impregnate in the pore channels of SBA-15 reduces further. During the calcination stage, the precursor salts of $SnCl_2{\bullet}2H_2O$, $TiCl_4$ and $AgNO_3$ were converted to their respective SnO_2, TiO_2 and Ag species. In the 'template removal' process, the SBA-15 material gets removed and the system is left with TiO_2/SnO_2 decorated with Ag nanoparticles.

Fig. 2(a) shows the small-angle XRD patterns of S-15, TS-s, TS-h and ATS-h. For sample S-15, a broad peak at 2θ = 0.8° (corresponding to (100) reflections) and two shoulder peaks in the 2θ region of 1−2° reveals the hexagonal mesoporous structure with *p6mm* symmetry

and long range ordering of mesoporous structure of SBA-15 template.[31] For the nanocomposite sample TiO_2/SnO_2 (TS-s) synthesized using soft templates, the peak at 2θ = 0.8° indicates the disordered mesoporous structure of the sample. However, the nanocomposites synthesized using hard templates, TS-h and ATS-h, shows a similar peak between 2θ = 0.8 - 0.9°, as exhibited by S-15. This peak corresponds to the (100) reflections of the *p6mm* space group and relates with the long range mesoporous structure of the nanocasted samples.[13] A right ward shift in peak at 2θ = 0.8° towards higher angles was observed in sample ATS-h as compared to TS-h, which can be related to the reduction in X-ray scattering contrast between pore channels and loading of Ag nanoparticles in the mesoporous framework. The information acquired from LAXRD results is listed in Table -1.

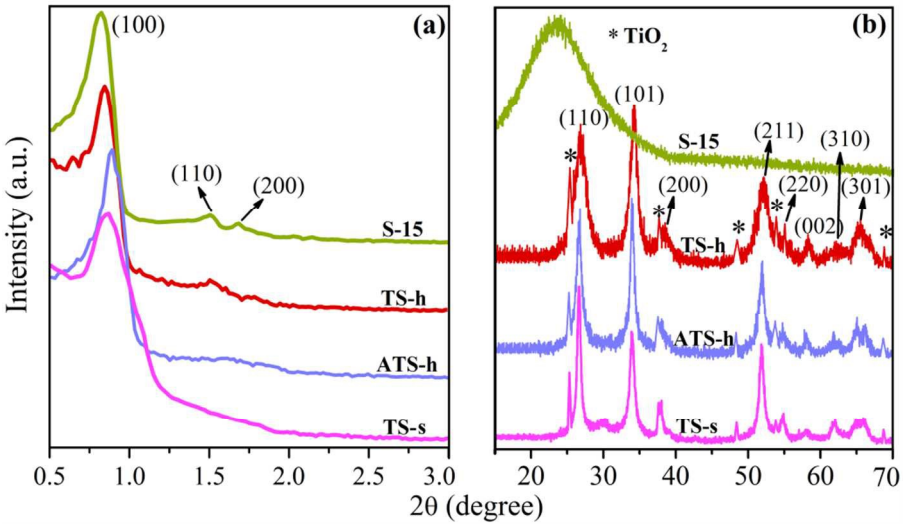

Fig 2: (a) LAXRD spectra (2θ range 0.5–3.0°) and **(b)** XRD spectra in (2θ range 15–70°) for samples S-15, TS-s, TS-h and ATS-h

Fig. 2(b) shows the wide angle XRD pattern (2θ = 15° - 70°) for samples S-15, TS-s, TS-h and ATS-h. For S-15, a broad peak centered at 2θ = 22° corresponding to the pristine material was observed. For samples TS-s, TS-h and ATS-h, well resolved peaks of tetragonal rutile SnO_2 crystal structure were observed at 2θ = 26.9°, 34.2°, 38.2°, 52.3°, 54.9°, 57.8°, 62.2°, 64.6° and 66.2° corresponding to (110), (101), (200), (211), (220), (002), (310), (112) and (301) planes

respectively, which was consistent with the standard data file (JCPDS no. 03-1116). No obvious characteristics peaks are observed for the impurities. Small diffraction peaks of anatase TiO_2 characteristic peaks were also observed at 2θ = 25.3°, 37.6°, 48.4°, 53.8° and 68.7° corresponding to (101), (004), (200), (105) and (116) planes. No characteristic diffraction peaks of Ag, Ag_2O or Ag_2O_3 in the sample ATS-h was observed, which could be due to the low amounts of Ag doped in the mesoporous TiO_2/SnO_2 or a homogeneous distribution of Ag nanoparticles.

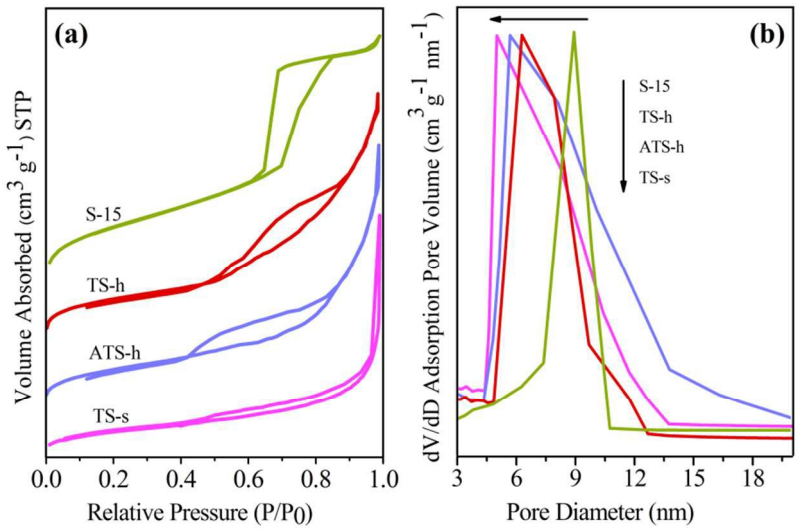

Fig 3: **(a)** N_2 adsorption-desorption isotherms curves and **(b)** Pore size distributions curves for S-15, TS-s, TS-h and ATS-h materials.

N_2 physisorption measurements and pore size distributions curves of S-15, TS-s, TS-h and ATS-h materials are shown in Fig. 3(a) and Fig. 3(b) respectively. The adsorption-desorption isotherms for SBA-15 template in Fig 3(a) displays type IV isotherms with H1-type hysteresis loops at the high relative pressure according to the IUPAC classification, which represents the characteristic of capillary condensation within uniform pores.[31] A steep increment in $P/P_0 > 0.6$ denotes a steep jump in the adsorption of nitrogen and confirms the co-existence of a mesoporous structure and a narrow pore size distribution of sample S-15. For the nanocomposite samples TS-s, TS-h and ATS-h, a type IV with a H3 hysteresis loop was observed.[31] A linear

increment in the slope from P/P_0 = 0.6 to 0.9 was observed which corresponds to the capillary condensation of N_2 in the mesoporous structure and related to the substantial interparticle porosity and irregular pores of gas bubbles. The surface area, pore size and pore volume information are summarized in Table-1. Comparatively, TiO_2/SnO_2 synthesized using nanocasting of SBA-15 possesses higher specific surface area than TiO_2/SnO_2 synthesized using PEG. The capillary condensation of TS-h occurs at a higher relative pressure (P/P_0 ~ 0.99) than that of TS-s, indicating much larger mesoporous diameters, a fact also validated by the pore diameter calculated using the desorption branch of the nitrogen adsorption isotherm (Table 1).

Sample	S_{BET} (m^2/g)[a]	D_P (nm)[b]	V_P (cm^3/g)[c]
S-15	872	8.98	1.31
TS-s	21	5.01	0.19
TS-h	78	6.32	0.33
ATS-h	49	5.74	0.26

[a] S_{BET}: Total surface area; [b] D_P: Pore size; [c] V_P: Pore volume

Table 1: Physiochemical properties of S-15, TS-s, TS-h and ATS-h materials

The morphologies and structures of the S-15, TS-s, TS-h and ATS-h were characterized by HRTEM analysis. Fig 4(a-c) shows the presence of long range of ordered pore channels along with 2D *p6-mm* regular hexagonal mesostructure for S-15 template. The strip-like channels are the characteristic (001) direction of the one-dimensional channels templated by the block copolymer P123.[13] A similar pattern of pore channels was observed for TS-h and ATS-h in Fig 4(d-f) and Fig 4(g-i) respectively, demonstrating that the nanocasted sample retains the inverse replica of the mesoporous S-15 template. The white and black lines in nanocasted samples correspond to mesoporous tubes and TiO_2/SnO_2 nanorods respectively. Fig 4(i) illustrates the highly distributed Ag nanoparticles (somewhere short 'nanorods') within the pore channels of TiO_2/SnO_2 nanocomposite. Fig 4(j,k) and Fig. 4(l,m) shows the HRTEM and FESEM images of

TiO_2/SnO_2 nanocomposite synthesized using conventional surfactant. As can be seen in FESEM images, a beautiful hierarchical flower like morphology was obtained. The EDX spectra of S-15 and ASn(h) are shown in Fig 5(a) and Fig 5(b) respectively. Strong signals of elemental Si, O, Sn and weak signal of Ag was detected for mesoporous SBA-15 template and Ag/SnO_2 indicating the phase purity of synthesized material.

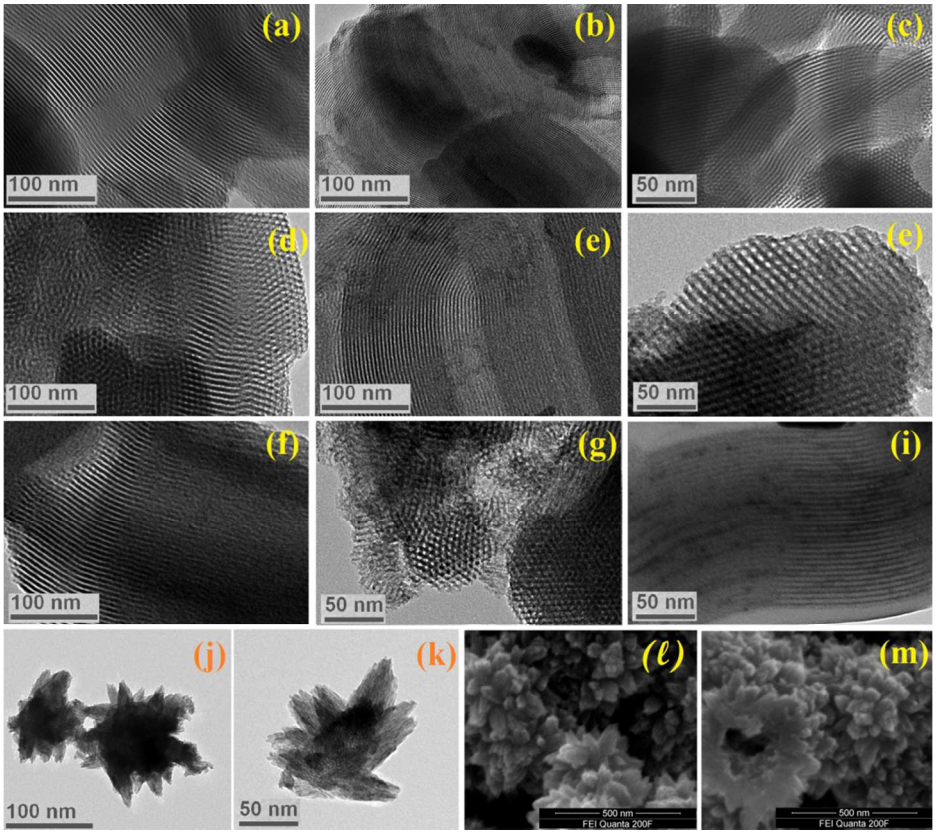

Fig 4: HRTEM image showing uniform channels with long range order of, **(a, b, c)** S-15 material; **(d, e, f)** TS-h material; **(g, h, i)** ATS-h material; **(j,k)** TS-s material and **(l,m)** FESEM images of TS-s material.

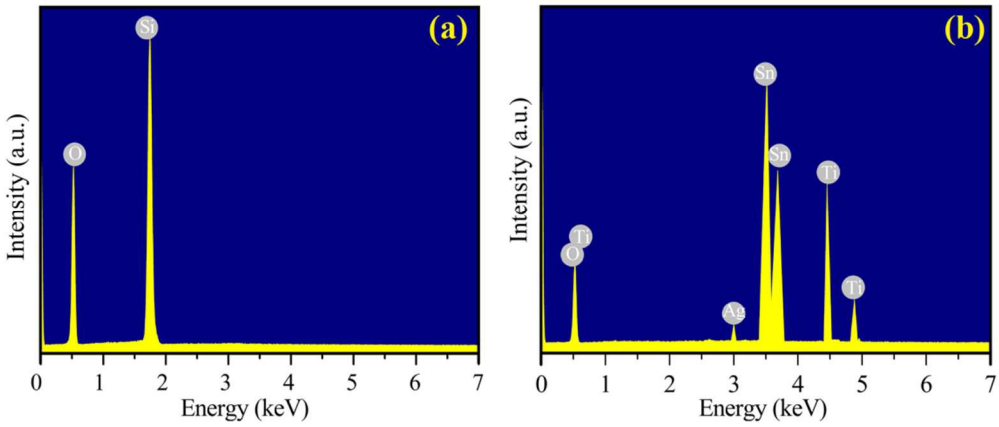

Fig 5: EDX spectra of **(a)** S-15 hard template and **(b)** ATS-h material

The valence states of O, Sn, Ti and Ag in the surface region of Ag-(TiO_2/SnO_2) were studied by XPS spectroscopy. Fig 6(a) shows that the O 1s profile is asymmetric and indicates the presence of physically adsorbed oxygen.[35] The XPS spectra for Sn 3d in Fig 6(b) illustrates the spin orbital splitting of the Sn^{4+} $3d_{3/2}$ and Sn^{4+} $3d_{5/2}$ core level states of tin centered at 495.7 and 487.3 eV, respectively and are assigned to the lattice of tin oxide. Also, the difference between the Sn $3d_{5/2}$ and Sn $3d_{3/2}$ level (8.4 eV) corresponds to the standard spectrum of Sn as reported in the Handbook of X-ray Photoelectron Spectroscopy.[36] Fig. 6(c) presents the XPS spectra of Ti 2p, and the peak positions of Ti $2p_{3/2}$ and Ti $2p_{1/2}$ located at 463.9 eV and 458.4 eV. Comparing the peak positions in standard literature, we can conclude that Ti element is in the state of Ti^{4+}.[36] The results also suggest a good coupling between SnO_2 and TiO_2. Fig. 6(d) shows the XPS spectra of Ag 3d in the hybrid nanocomposite. As can be seen, two peaks locating at 373.9 and 367.9 eV corresponding to Ag $3d_{3/2}$ and Ag $3d_{5/2}$, respectively were observed. These two peaks can be related to metallic Ag (Ag^0).[37] On comparing with the binding energy for pure metallic Ag (368.2), a negative shift in binding energy peaks of Ag $3d_{5/2}$ was observed which could be due to the strong interaction between Ag and TiO_2/SnO_2.[38]

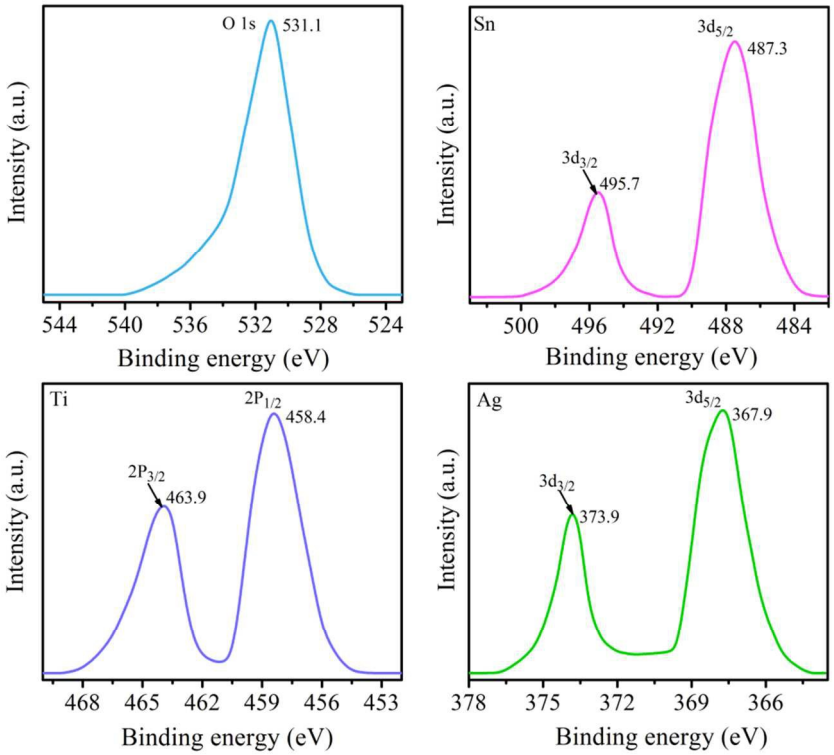

Fig. 6: XPS spectra of Ag-(TiO_2/SnO_2). **(a)** O 1s, **(b)** Sn 3d, **(c)** Ti 2p and **(d)** Ag 3d.

Gas sensing properties

Growing concern on environmental monitoring for detecting VOCs as indoor air pollutant has led to an upsurge interest in development of fast and highly efficient gas sensors. Semiconducting metal oxides with heterojunction and additional provision of high intrinsic surface area with ordered porous structure have been proven to significantly enhance gas-sensing properties and are promising materials for gas sensor. Considering the dependency of gas sensor sensitivity on the operating temperature, the responses of as synthesized sensors, S-15, TS-s, TS-h and ATS-h towards 50 ppm ethanol in temperature range 150–400 °C are tested. As observed in Fig. 7, pure S-15 template shows no response towards ethanol gas in the test temperature range, however, the gas sensor based on TiO_2/SnO_2 nanocomposite prepared using soft template shows a maximum response of 14 at 275 °C. In the case of the sensor TiO_2/SnO_2, synthesized using nanocasting of SBA-15, a maximum response of 38 was obtained at 275 °C. It can be clearly seen that the high intrinsic surface area and long/ordered pore channels of the

mesoporous nanocomposite increases the ethanol sensing response ~ 2.7 times than conventional surfactant assisted nanocomposite. For Ag doped mesoporous TiO_2/SnO_2, the response rises monotonically in the range of 200–275 °C and reaches the maximum response of 53 at 275°C then decrease with a further increase of the operating temperature. The poor response of gas sensor at low and high operating temperatures could be due to the slow chemical activation and the tendency of gas molecules to escape from chemical reactions, respectively.[39] Overall, the response of the sensor, ATS-h to ethanol gas was ~1.4 and 3.7 times higher than sensor TS-h and TS-s respectively at the same temperature. This operating temperature of 275 °C could be useful for an improved selectivity of ethanol.

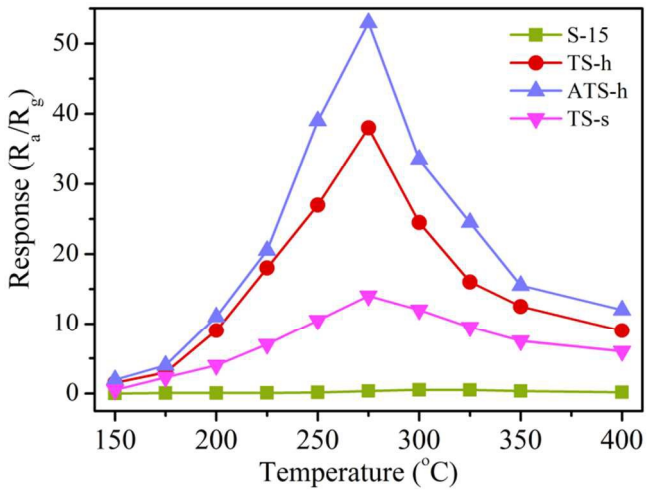

Fig. 7: Responses of S-15, TS-h, ATS-h and TS-s materials to 50 ppm ethanol at different operating temperatures (150–400 °C).

Fig. 8 illustrates the response of the as synthesized sensors based on S-15, TS-s, TS-h and ATS-h materials against different concentrations of ethanol gas (1, 5, 10, 30, 50, 75, 100, 200, 300, 400 and 500 ppm) at fixed working temperature of 275 °C. As observed, the sensor based on mesoporous TS-h nanocomposite shows relatively higher response then the sensor TS-s at each concentration level. The sensor ATS-h shows highly linear response with concentrations

increasing from 1 to 500 ppm. An enlarged view of all the materials in 1-50 ppm ethanol concentration range in inset of Fig. 8 also shows the excellent linearity of the ATS-h sensor.

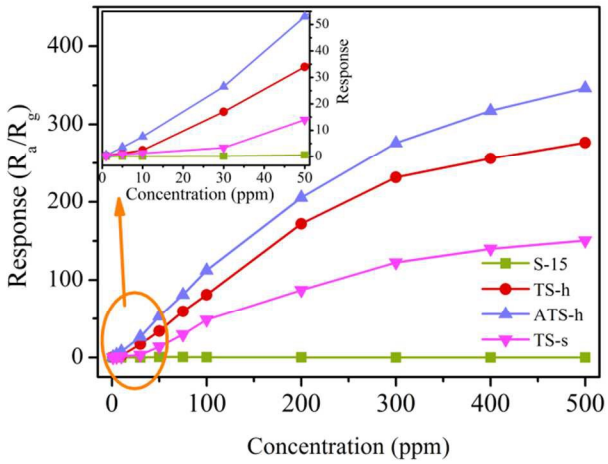

Fig. 8: Responses of the sensors based on S-15, TS-h, ATS-h and TS-s materials to ethanol in the range from 1–500 ppm at 275 °C (the inset shows the calibration curve in the range of 1–50 ppm).

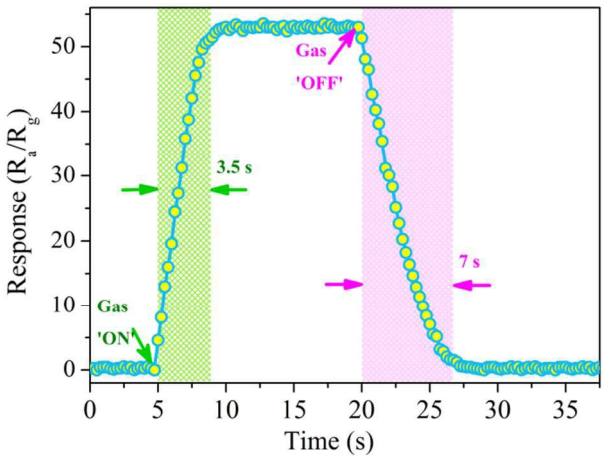

Fig. 9: The response and recovery of mesoporous ATS-h to 50 ppm ethanol at 275 °C.

Response and recovery times are very important basic parameters to determine the working of a sensor in real time fast changing environment. A sensor with swift response and rapid recovery time usually made it an excellent real-time detector and found excellent usage in practical applications. Response and recovery times of gas sensors are usually defined as the time required while reaching 90% of the final resistance in case of the process of adsorption and desorption respectively.[13] Fig. 9 shows a single cycle response-recovery behavior of the Ag

doped mesoporous TiO_2/SnO_2 nanocomposite to 50 ppm ethanol operating at 275 °C. The response and recovery time are recorded to be 3.5 s and 7 s, respectively. A comparison with other reported materials (Table – 2) shows that our sensor responds profoundly faster than other SnO_2 and metal oxide based ethanol sensor.

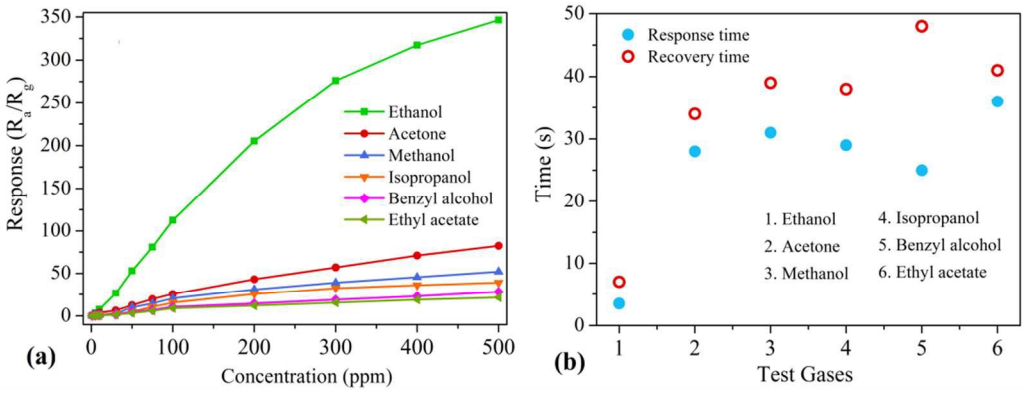

Fig. 10: (a) The response of ATS-h versus varying concentration of test gases, **(b)** The response and recovery times of mesoporous ATS-h to 50 ppm test gases at 275 °C.

Fig. 10(a) illustrates the response of the sensor ATS-h versus varying concentrations of test gases (ethanol, acetone, methanol, isopropanol, benzyl alcohol and ethyl acetate) at 275 °C operating temperature. It is obviously observed from the calibration curves that the response of sensor ATS-h increases linearly with the increase of test gas concentration (1 – 500 ppm). Among all the test gases, the sensor responded excellently towards ethanol gas, which might be owed to the easier oxidization of hydroxyl group at that condition. Fig 10(b) shows the response and recovery times of ATS-h sensor towards detection of 50 ppm test gases at 275 °C operating temperature. As can be seen, the response/recovery time (3.5/7 s) for the nanocasted Ag doped mesoporous TiO_2/SnO_2 nanocomposite towards detection of ethanol gas is significantly less than that for acetone (28/34 s), methanol (31/39 s), isopropanol (29/38), benzyl alcohol (25/48 s) and ethyl acetate (36/41 s), illustrating that the sensor ATS-h respond quickly to ethanol gas under same test conditions.

S. No.	Material	Synthesis route/ morphology	Concentration (ppm)	Response	Operating temperature (°C)	Response/ Recovery time (s/s)	Ref
1	SnO_2/ZnO	Thermal evaporation and hydrothermal / hierarchical nanostructures	100	6	400	N.M.	7
2	SnO_2/ZnO	Electrospinning/ nanofibers	100	78	300	25/9	8
3	Ni/SnO_2	Hydrothermal/hollow spheres	100	59	280	2/15	20
4	Zn/SnO_2	Carbon template/ microspheres	100	28	240	7/4 (2 ppm)	21
5	SnO_2	Hydrothermal/nanosheets	60	10	275	11/125	22
6	α – Fe_2O_3/ SnO_2	Hydrothermal/ core shell nanostructure	100	18.4	225	1/31	24
7	SnO_2	Hydrothermal/nanoflowers	500	12.2	240	25/60	25
8	Carbon assisted SnO_2	Hydrothermal/nanospheres	10	4.5	300	5/20	26
9	SnO_2	Hydrothermal/microcubes	100	45.2	280	13/51	27
10	ZnO/TiO_2	Electrospinning, Hydrothermal/ nanorods	500	50.6	320	5/10	40
11	Aloe like SnO_2	Hydrothermal/nanoflowers	50	23	285	1.2/76	43
12	SnO_2	Hydrothermal	50	25	300	1/9	44
13	Pd/Fe_3O_4	Hydrothermal/nanoparticle	100	27*	300	18/30 (40 ppm)	45
14	In/SnO_2	Flame spray pyrolysis/ nanoparticle	1000	110	300	2/N.M.	46
15	Co/In_2O_3	Electrospinning/ nanofiber	100	16.5	300	2/3	47
16	Ag-(TiO_2/ SnO_2)	Hydrothermal and nanocasting/ order mesoporous nanostructures	50	53	275	3.5/7	TW

* Calculated from given results; NM: not mentioned; TW: this work

Table 2: A comparison of ethanol sensing performance based on different semiconducting metal oxide materials.

The dynamic response versus time curves of ATS-h sensor to different concentrations of ethanol is shown in Fig. 11. For ethanol gas at levels of 1, 5, 10, 30, 50, 75 and 100 ppm, the responses are about 3, 5, 8, 27, 53, 81 and 112, respectively. From the above results, it is clearly seen that sensor responses towards detection of ethanol increase with increasing of the analyte concentrations. The real time response curves also suggest that the ATS-h sensor has excellent response, reversibility and stability. Once the fresh air was flown in the chamber, the response of

the sensor returned to baseline quickly. An enlarged view of ATS-h sensor response towards 1 ppm ethanol gas is shown in inset of Fig 11(a). The sensor ATS-h can detect ethanol down to 1 ppm (the corresponding response is 3). A standard deviation of 0.63 % (Fig 11 (a)) and 0.74% (Fig 11 (b)) was obtained when the sensor came in contact with the varying concentrations of ethanol gas. The result shows that the sensing response is highly repeatable. Such excellent ethanol sensing properties can be attributed to the unique mesoporous structure of the nanocomposite.

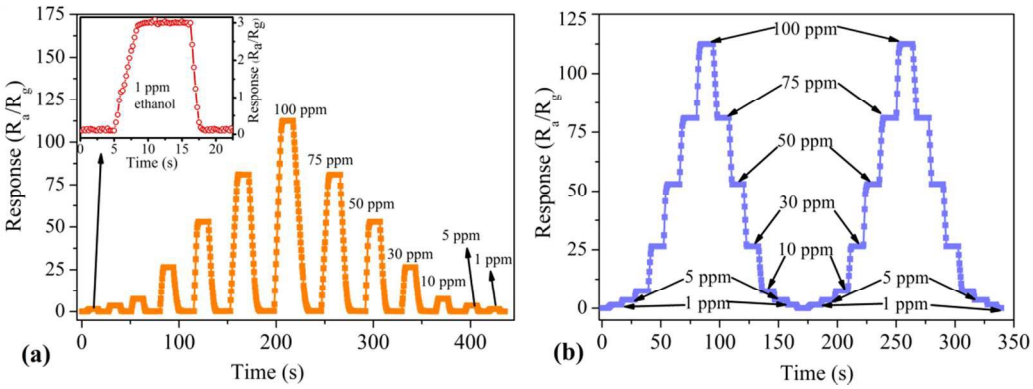

Fig 11: Typical real time response curves of gas sensors based on ATS-h materials when exposed to different concentrations of ethanol (1-100 ppm) at a working temperature of 275 °C. Inset in Fig 11(a) shows the response of ATS-h sensor to 1 ppm ethanol gas at 275 °C.

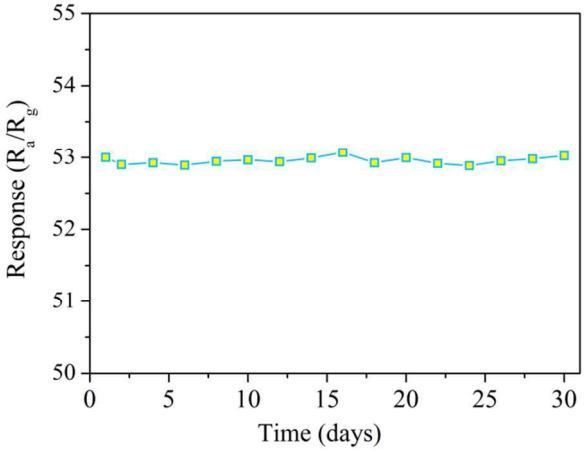

Fig 12: The long-term stability of mesoporous ATS-h to 50 ppm ethanol at 275 °C.

The long-term stability of the sensor is considered a vital characteristic in terms of practical applications. Therefore, tests of the ATS-h response toward 50 ppm ethanol at 275 °C

were carried out at alternate days as shown in Fig. 12. It can be noted that the sensors exhibit nearly constant response signals without an obvious increase/decrease even after 30 days, while recording a standard deviation of 0.8%. The result further confirmed that the present sensor possess excellent stability.

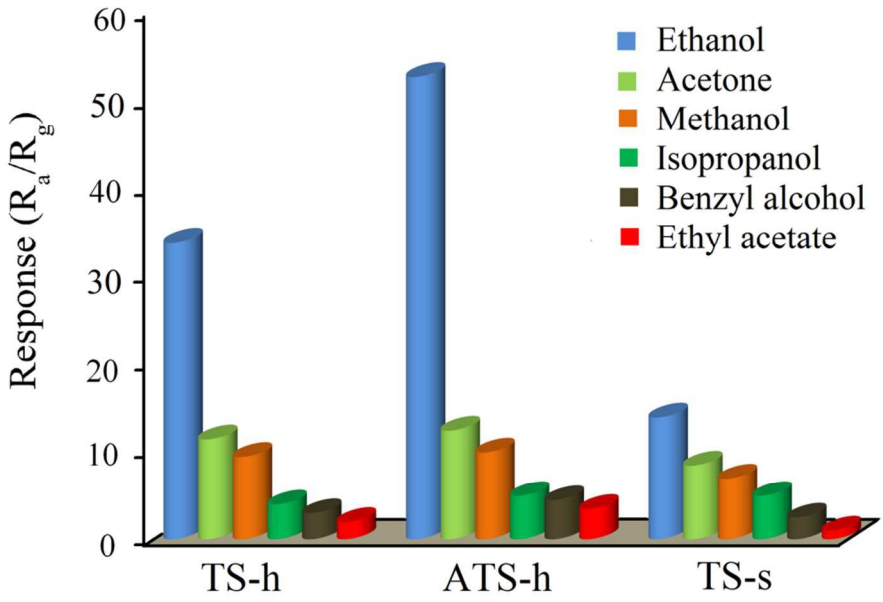

Fig 13: Responses of TS-h, ATS-h and TS-s materials to 50 ppm test gases

The great selectivity is additionally an essential property of a gas sensor when it is recognizing a target gas in the vicinity of multi-gas particles, particularly those with comparative physicochemical properties. In this work, the selectivity of nanocomposite samples (TS-h, ATS-h and TS-s) are tested by exposing them to 50 ppm different gases, including ethanol (C_2H_5OH), acetone (CH_3COCH_3), methanol (CH_3OH), isopropanol ($CH_3CHOHCH_3$), benzyl alcohol ($C_6H_5CH_2OH$) and ethyl acetate ($CH_3COOCH_2CH_3$) at 275 °C. As can be observed in Fig. 13, the mesoporous ATS-h exhibits undoubtedly the strongest sensitivity among the three gas sensors. It is worth noting that the response shown by ATS-h to ethanol (53) is 4 times larger than acetone (12.5) and 5.3 times larger than methanol (10). The sensor, ATS-h shows relatively poor responses to isopropanol, benzyl alcohol and ethyl acetate. This could be due to different

volatilities and chemical properties of VOCs which prompts the sensor to exhibit different adsorption and catalytic performances towards them.[8]

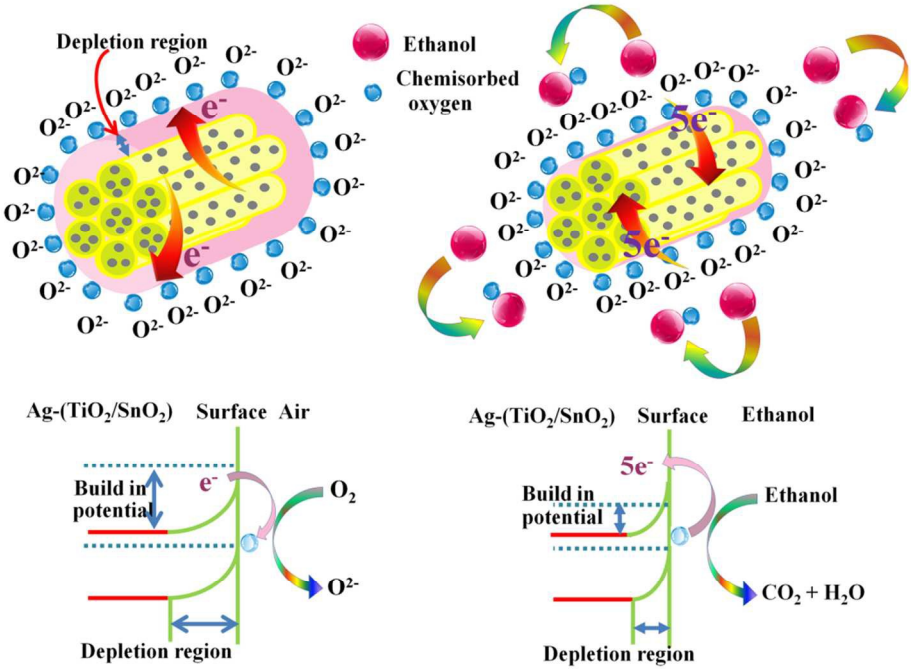

Fig 14: A schematic of ethanol sensing mechanism by Ag-(TiO_2/SnO_2) material.

Ethanol sensing mechanism

The fundamental mechanism of sensing by porous semiconducting metal oxide has been discussed in details in the literature.[20-22] In semiconducting metal oxides, the sensing proceeds from the interaction of gas molecules with the surface of materials thereby leading to a change in its electrical conductivity. The enhanced sensitivity of mesoporous materials is attributed to their unique porous structure having high specific surface area along with ordered and long range mesoporous channels. The sensing mechanism involves mainly gas adsorption, charge transfer and desorption.[23,29,32] When the sensor ATS-h is exposed to hot air at 275 °C, the oxygen molecules in air traps free electron from the conductance band of n-type sensing layer of TiO_2 and SnO_2 thereby leading to the formation of O^-, O^{2-}, O_2^-, and O_2^{2-}. This trapping of the electrons causes electron depletion layer and a space charge region is formed on the surface of sensor and increases its resistance.[40] The target gas molecules get preferably adsorbed on these oxygen sites.

The ethanol gas when introduced to the sensor surface gets oxidized by reactive oxygen species and electrons are released resulting in the increase in conductivity of the ATS-h sensor. A schematic of gas sensing mechanism for ATS-h material is shown in Fig 14. Sensor performance towards a target gas in mesoporous semiconducting metal oxides primarily depends upon the factors including formation of heterojunction in sensor, nature of target gas and surface area of the sensor. In this study, the presence of mixed oxide heterostructures (TiO_2/SnO_2) causes the electron transport to precede through different potential barriers namely TiO_2 and TiO_2, TiO_2 and SnO_2, and SnO_2 and SnO_2. Due to the higher Fermi level of TiO_2 than SnO_2, the electrons are transferred from TiO_2 to SnO_2 by band bending thus creating a potential barrier between the heterojunction. These potential barriers cause a hindrance in the electron transportation through the nanostructures and the electrons present on the sensor surface becomes obvious choice for oxygen species to get adsorb upon which significantly increases the sensor response.[1]

The gas sensing performance is highly dependent upon the surface reactions between the target gas and adsorbed oxygen species. SnO_2 has both acidic and basic properties while TiO_2 is basic in nature. And so, the addition of TiO_2 in SnO_2 increases the basicity of the composite and the dehydrogenation of ethanol gas takes place according to equation $C_2H_5OH \rightarrow CH_3CHO + H_2$. The CH_3CHO then react with oxygen ions to produce CO_2 and H_2O ($CH_3CHO + 5O^- \rightarrow 2CO_2 + 2H_2O + 5e^-$), where also the electrons are generated in the system and decreases the resistance of the sensor. Porosity of the material is another important factor that governs the sensitivity of the sensor. As compared to the nanocomposites synthesized using conventional surfactants (TS-s), the hard templated negative replicated nanocomposites (TS-h and ATS-h) shows enhanced specific surface area with well ordered/long pore channels. Therefore, the sensing film based on the ordered mesoporous TiO_2/SnO_2 nanocomposite with more active sites becomes favorable for the diffusion and rapid transmission of gas molecules across the sensor surface, and become the

deciding factor for determining the sensitivity and response time of the gas sensor. Although, the effective surface area of as-synthesized samples is highly interrelated to the surface morphology, the sensing behavior of samples is found to be not directly depended on the surface area. The sample ATS-h has less surface area but shows 1.5 times better response than TS-h nanocomposite because some of the surface area of TS-h was sacrificed for making the room for Ag nanoparticles and resulting in the significant improvement in response of the ATS-h material.

The role of Ag nanoparticles becomes important in enhancing the gas sensing performances of metal oxide nanocomposites. The presence of Ag nanoparticles favors the gas sensing response by the process of chemical sensitization, catalytic oxidation (spill-over effect), resulting in increasing the quantities of active oxygen species on the surface of TiO_2/SnO_2 nanocomposite.[41] Ag nanoparticles facilitate the faster adsorption and desorption of the oxygen molecules (O_2) over the sensor surface and capture electrons from the conduction bands of both TiO_2 and SnO_2 to become oxygen ions (O^-). This process promotes the quantity of adsorbed O_2 molecules and enhances the molecule-ion conversion rate, and leads to the quick changes in the height of the barrier potential at TiO_2/SnO_2 interfaces. The catalytic nature of Ag nanoparticles promotes the disintegration of ethanol into active radicals and increases the reaction between adsorbed surface oxygen ions and ethanol gas.[42] Moreover, the metal nanoparticles act as efficient electron sinks due to their large Helmholtz double layer. Hence, the Ag nanoparticles adopt a tendency to form Ag_2O compound in air and promotes the development of a more intense e- depleted layer in the course of extraction of e- from both TiO_2 and SnO_2. These trapped e^- are released back to TiO_2 and SnO_2 via a redox reaction between Ag_2O and Ag on exposure to reductive ethanol gas.[41] Due to the lower work function of Ag than TiO_2 and SnO_2, e- from the Ag move on to the TiO_2/SnO_2 heterojunction thus leading to the formation of an accumulation of a negative charge layer around the Ag and TiO_2–SnO_2 interface. This process

then facilitate the dissociative adsorption of oxygen on the TiO_2–SnO_2 surface thereby enhancing the formation of electron charge transfer dynamics between the ethanol gas molecules and the sensor surface. In this way, the regions adjacent to the Ag and TiO_2/SnO_2 interface make the sensors more sensitive for ethanol gas detection. A comparison between the sensing performances of the sensor and literature reports is summarized in Table–2. It is note worthy that the sensor fabricated in our work exhibits better sensing performances compared with those reported in the literature due to the formation of unique heterojunction and high internal specific surface area.

Conclusion

In summary, a robust, highly sensitive, reliable and reproducible ethanol sensor was fabricated by utilizing mesoporous Ag doped TiO_2/SnO_2 nanocomposite synthesized using hard template of SBA-15 via the nanocasting process. The uniqueness of mesoporous structure is the availability of high intrinsic surface area, large pore channels diameter/volume and can be understood from the 3 times higher response (ethanol gas, 50 ppm@ 275 °C) of nanocasted mesoporous TS-h (R = 38) than the nanocomposite synthesized using conventional surfactant, TS-s (R = 14). The Ag doping further enhances the response of TS-h by 1.5 times (R = 53) along with very fast response (3.5 s) and recovery times (7 s). It also shows excellent stability, selectivity and a very low detection limit (1 ppm) for ethanol. The present work suggests that the mesoporous structure of the sensor improves the adsorption efficiency of ethanol molecules and facilitates the propagation of charge carriers across its surface. From the investigation results, the as-fabricated chemoresistive sensor using the highly ordered mesoporous hybrid metal oxide presented a strategy to develop highly sensitive gas sensors with high stability, short response/recovery times and selectivity for utilization in biomedical and environmental applications both in terms of cost effectiveness and performance.

Acknowledgements

Authors are grateful to UGC, New Delhi (Grant No. 41-997/2012(SR)) for providing financial assistance. Authors are also thankful to Dr. I.S. Mulla (Emeritus scientist, CSIR, India) for his thoughtful and valuable suggestions.

References

[1] A. K. Nayak, R. Ghosh, S. Santra, P. K. Guha and D. Pradhan, *Nanoscale*, 2015,**7**, 12460-12473

[2] Z. Guo, Z.-W. Jiang, X.Chen, B. Sun, M.-Q. Li, J.-H. Liu and X.-J. Huang, *J. Mater. Chem.*, 2011, **21**, 1874-1879

[3] P. Mochalski, J. King, M. Klieber, K. Unterkofler, H. Hinterhuber, M. Baumann and A. Amann, *Analyst*, 2013, **138**, 2134-2145

[4] A. Mazzatenta, M. Pokorski, F. Sartucci, L. Domenici and C. D. Giulio, Respiratory Physiology & Neurobiology, 2015, **209**, 81–84

[5] M. Kimura, R. Sakai, S. Sato, T. Fukawa, T. Ikehara, R. Maeda and T. Mihara, *Adv. Funct. Mater.* 2012, **22**, 469–476.

[6] F. Caldararu, C. Vatra and M. Caldararu, *J. Environ. Monit.*, 2012, **14**, 2616-2623

[7] N. D. Khoang, D. D. Trung, N. V. Duy, N. D. Hoa and N. V. Hieu, *Sens Actuators B*, 2012, **174**, 594–601

[8] S.H. Yan, S.Y. Ma, W.Q. Li, X.L. Xu, L. Cheng, H.S. Song and X.Y. Liang, *Sens Actuators B* 2015, **221**, 88–95

[9] S. Duhan and V. K. Tomer Mesoporous Silica: Making "Sense" of Sensors. In: A. Tiwari, M. M. Demir, editors. Advanced Sensor and Detection Materials, Wiley-Scrivener Publishing 2014 p. 149-92.

[10] V. K. Tomer and S. Duhan, *Sens. Actuators B*, 2015, **220**, 192–200

[11] V. K. Tomer and S. Duhan, *App. Phy. Lett.*, 2015, **106**, 063105

[12] Y. Weng, L. Zhang, W. Zhu and Y. Lv, *J. Mater. Chem. A*, 2015, **3**, 7132

[13] X. Lai, G. Shen, P. Xue, B. Yan, H. Wang, P. Li, W. Xia and J. Fang, *Nanoscale*, 2015, **7**, 4005-4012

[14] V. K. Tomer and S. Duhan, *Sens Actuators B,* 2016, **223**, 750

[15] S. Vetter, S. Haffer1, T. Wagner and M. Tiemann, *Sens. Actuators B,* 2015, **206**, 133–138

[16] Y. Ren, Z. Ma and P. G. Bruce, *Chem. Soc. Rev.*, 2012, **41**, 4909-4927

[17] S. Lepoutre, B. J. López, C. Sanchez, H. Amenitsch, M. Linden and D. Grosso, *J. Mater. Chem.*, 2010, **20,** 537-542

[18] E. Skliri, I. N. Lykakis and G. S. Armatas, *RSC Adv.,* 2014, **4**, 46170

[19] J. Zhao, W. Wang, Y. Liu, J. Ma, X. Li, Y. Du and G. Lu, *Sens Actuators B,* 2011, **160**, 604

[20] Y. Chen, L. Yu, D. Feng, M. Zhuo, M. Zhang, E. Zhang, Z. Xu, Q. Li and T. Wang, *Sens. Actuators B,* 2012, **166**, 61-67

[21] W. Wang, Y. Tia, X. Li, X. Wang, H. He, Y. Xu and C. He, App. Surface Science, 261 (2012) 890

[22] P. Sun, X. Mei, Y. Cai, J. Ma, Y. Sun, X. Liang, F. Liu and G. Lu, *Sens. Actuators B,* 2013, **187**, 301-307

[23] T. Rakshit, S. Santra, I.Manna and S. K. Ray, *RSC Adv.*, 2014, **4**, 36749-36756

[24] P. Sun, C. Wang, J. Liu, X. Zhou, X. Li, X. Hu, and G. Lu, *Appl. Mater. Interfaces*, 2015, **7**, 19119–19125

[25] L. Wang, S. Wang, Y. Wang, H. Zhang, Y. Kang and W. Huang, *Sens. Actuators B,* 2013, **188**, 85-93

[26] X. Feng, J. Jiang, H. Ding, R. Ding, D. Luo, J. Zhu, Y. Feng and X. Huang, *Sens. Actuators B*, 2013, **183**, 526

[27] J. Huang, L. Wang, C. Gu, Z. Wang, Y. Sun and J.-J. Shim, *Sens. Actuators B,* 2015, **207**, 782-790

[28] M. Radecka , A. Kusior, A. Lacz, A. T.-Zajac, B. L.-Sypien and K. Zakrzewska, *J. Thermal Analysis and Calorimetry*, 2012, **108**, 1079-1084

[29] W. Zeng, T. Liu and Z. Wang, *J. Mater. Chem.*, 2012, **22**, 3544-3548

[30] V. K. Tomer, S. Duhan, A. K. Sharma, R. Malik, S. Jangra, S. P. Nehra, S. Devi, *Eur. J. Inorg. Chem.,* 2015, **2015**, 5232

[31] V. K. Tomer, S. Devi, R. Malik, S.P. Nehra and S. Duhan, *Micro. Meso. Mat.* 2016, **219**, 240

[32] Y. Zeng, T. Zhang, L. Wang, M. Kang, H. Fan, R. Wang and Y. He, *Sens. Actuators B*, **140**, 73-78

[33] S. Brunauer, P. H. Emmet and E. Teller, *J. Am. Chem. Soc.,* 1938, **60**, 309.

[34] E. P. Barrett, L. G. Joyner and P. P. Halenda, *J. Am. Chem. Soc.,* 1951, **73**, 373.

[35] J. F. Moudler, W. F. Stickle, P. E. Sobol and K. D. Bomben, Handbook of X-ray Photoelectron Spectroscopy, ed. J. Chastain, R. C. King Jr., Physical Electronics Division, Perkin-Elmer Corp, Eden Prairie, MN, 1995, p. 127.

[36] C. D. Wagner, W. M. Riggs, L. E. Davis and J. F. Moulder, Handbook of X-ray Photoelectron Spectroscopy, Perkin Elmer, Eden Prairie, 1979, p. 81.

[37] H. Zhang, G. Wang, D. Chen, X. J. Lu and J. H. Li, *Chem. Mater.,* 2008, **20**, 6543.

[38] C. Ren, B. Yang, M. Wu, J. Xu, Z. Fu, Y. Lv, T. Guo, Y. Zhao and C. Zhu, *J. Hazard. Mater*., 2010, **182**, 123.

[39] H. Ren, W. Zhao, L. Wang, S. O. Ryu and C. Gu, *J. Alloys Compounds,* 2015, **653**, 611-618

[40] J. Deng, B. Yu, Z. Lou, L. Wang, R. Wang and T. Zhang, *Sens. Actuators B,* 2013, **184**, 21

[41] L. Xu, R. Xing, J. Song, W. Xu and H. Song, *J. Mater. Chem. C,* 2013, **1**, 2174

[42] Z. Zhang, H. Song, S. Zhang, J. Zhang, W. Bao, Q. Zhao and X. Wu, *Cryst Eng Comm*, 2014, **16**, 110-115

[43] L. Mei, J. Deng, X. Yin, M. Zhang, Q. Li, E. Zhang, Z. Xu, L. Chen and T. Wang, *Sens. Actuators B,* 2012, **166**, 7

[44] Z. Lou, L. Wang, R. Wang, T. Fei and T. Zhang, *Solid-State Electronics,* 2012, **76**, 91-94

[45] Q. Zhai, B. Du, R. Feng, W. Xu and Q. Wei, *Anal. Methods*, 2014, **6**, 886-892

[46] K. Inyawilert, A. Wisitsoraat, C. Sriprachaubwong, A. Tuantranont, S. Phanichphant and C. Liewhiran, *Sens. Actuators B,* 2015, **209**, 40–55

[47] Z. Li and Y. Dzenis, *Talanta,* 2011, **85**, 82-85